



# GRB 190530A: From Precursor, Prompt Emission to Afterglow all Originated from Synchrotron Radiation

Hui-Ya Liu<sup>1,2</sup>, Xiang-Gao Wang<sup>1,2</sup> , Li-Ping Xin<sup>3</sup> , Zi-Min Zhou<sup>1,2</sup>, Liang-Jun Chen<sup>1,2</sup>, Bing Li<sup>4</sup> , Yuan-Gui Yang<sup>5</sup>, Qi Luo<sup>4</sup> , Cheng-Kui Li<sup>4</sup> , Shao-Lin Xiong<sup>4</sup> , Ling-Jun Wang<sup>4</sup> , Xu-Hui Han<sup>3</sup>, Li-Ming Song<sup>4</sup> , Jian-Yan Wei<sup>3</sup>, En-Wei Liang<sup>1,2</sup> , and Shuang-Nan Zhang<sup>4</sup> 

<sup>1</sup> Guangxi Key Laboratory for Relativistic Astrophysics, Department of Physics, Guangxi University, Nanning 530004, China; [wangxg@gxu.edu.cn](mailto:wangxg@gxu.edu.cn)

<sup>2</sup> GXU-NAOC Center for Astrophysics and Space Sciences, Nanning 530004, China

<sup>3</sup> CAS Key Laboratory of Space Astronomy and Technology, National Astronomical Observatories, Chinese Academy of Sciences, Beijing 100101, China

<sup>4</sup> Key Laboratory of Particle Astrophysics, Institute of High Energy Physics, Chinese Academy of Sciences, Beijing 100049, China

<sup>5</sup> School of Physics and Electronic Information, Huaibei Normal University, Huaibei 235000, China

Received 2022 March 1; revised 2022 March 31; accepted 2022 April 7; published 2022 May 20

## Abstract

GRB 190530A was jointly observed by the High Energy X-ray Telescope of the Hard X-ray Modulation Telescope (Insight-HXMT/HE) and the Ground-Based Wide-Angle Camera network (GWAC-N) with the extremely large field of view. After triggered by Insight-HXMT/HE and Fermi/GBM, we observed the optical emission of GRB 190530A, using the 30 cm telescope of GWAC (GWAC-F30) to search and locate its position. Subsequent observation of the late afterglow of GRB 190530A was made with the 2.16 m telescope at Xinglong Observatory. In this paper, we make a detailed exploration of the origin of GRB 190530A. In the prompt emission, a “double-tracking” pattern is presented both for the low-energy spectral index  $\alpha$  and the peak energy  $E_p$  in the Band function with Insight-HXMT/HE and Fermi/GBM data; the results of GRB 190530A are consistent with the Amati and Yonetoku correlations; the spectral lag ( $\tau$ ) versus energy ( $E$ ) can be estimated with  $\tau = -3.0 \pm 0.06 + (0.17 \pm 0.03)\log E$ . The synchrotron radiation can account for the origin of GRB 190530A prompt emission behaviors. The  $\alpha$  and  $E_p$  of the precursor are essentially the same as that of the main prompt emission, implying that they have the same origin. For the afterglow, it can be described with the external forward shock model in ISM circumburst medium. In summary, from precursor, prompt emission to afterglow of GRB 190530A all originated from synchrotron radiation.

*Key words:* (stars:) gamma-ray burst: individual (GRB 190530A) – (stars:) gamma-ray burst: general – virtual observatory tools

## 1. Introduction

Gamma-ray bursts (GRBs) in the universe were first discovered by the Vela military satellites. The distribution of GRBs across the sky is completely random. The energy of gamma photons ranges from 1 keV to several GeV and above, and the duration is usually from  $10^{-2}$  to  $10^3$  s. From observations, it can be found that there are basically two types of cosmic GRBs. One class of GRBs, called long-soft GRBs, last for more than 2 s, and gamma photons have lower energy. The other class, called short-hard GRBs, last for less than 2 s and are characterized by a higher gamma-photon energy. A long GRB is supposed to come from the core-collapse of a massive star (Woosley 1993; Paczyński 1998; MacFadyen & Woosley 1999; Kumar & Zhang 2015), and the theory is confirmed by the fact that some long GRBs are observed in association with supernovae. While short GRBs are believed to be the mergers of two compact stars (Paczynski 1986; Eichler et al. 1989; Narayan et al. 1992), the short GRB is associated with the

gravitational wave burst caused by the merger of two neutron stars, which confirms the origin model. The central engine of GRBs remains a long-lasting question in GRB physics, but two main contenders have been proposed for the central engine: a hyper-accreting stellar-mass black hole (e.g., Woosley 1993; Popham et al. 1999; Narayan et al. 2001; Liu et al. 2007, 2018; Lei et al. 2013; Song et al. 2016) or a newly formed, highly magnetized, millisecond neutron star (e.g., Usov 1992; Dai & Lu 1998; Spruit et al. 2001; Dai et al. 2006; Rowlinson et al. 2013, 2014; Lü & Zhang 2014; Zheng et al. 2021).

These events provided energy for a high-energy relativistic jet, which has powerful  $\gamma$ -ray radiation with an isotropic equivalent energy of  $\sim 10^{50}$ – $10^{54}$  erg. Observationally, most light curves exhibit rapid variability. Following the prompt  $\gamma$ -ray emission, the blast wave interacts with the circumburst medium and produces an afterglow emission (Paczynski & Rhoads 1993; Huang et al. 2018). With the launch of space observatory such as the Fermi (Meegan et al. 2009; Atwood et al. 2009) and Niel Gehrels Swift (Gehrels et al. 2004)

telescopes, the knowledge of the origin of the prompt emission and afterglow of GRBs has been improved significantly. However, the nature of the radiation mechanism still remains unclear. The non-thermal nature of the GRB spectra is generally interpreted in terms of radiation processes, such as synchrotron processes (Rees & Meszaros 1994; Li et al. 2020).

GRB 190530A is an interesting case, having a bright and long main prompt emission with a duration of about 16 seconds, and also a fainter precursor emission with a duration of about 5 seconds. The main prompt emission episode also has a complex structure and consists of several pulses. In this paper, we present the joint observation of GRB 190530A by the High Energy X-ray Telescope of the Hard X-ray Modulation Telescope (Insight-HXMT/HE) and the Ground-based Wide-Angle Camera Network (GWAC-N). Combining our data with other observations, we provide an analysis of the GRB 190530A from its precursor, prompt emission to afterglow. Our observations are presented in Section 2. The temporal characteristics analysis and detailed time-resolved spectral analysis of the multi-pulse in the prompt emission are performed in Section 3, where the evolution patterns of  $E_p$  and  $\alpha$  are also provided. The light curves during the X-ray and optical emission of this burst are analyzed in Section 4. Then, its physical interpretation for the evolution patterns of  $E_p$  and  $\alpha$  as well as the X-ray and optical emission are discussed in Section 5.

## 2. Observations and Data Reduction

### 2.1. Prompt Gamma-Ray Emission

GRB 190530A triggered Insight-HXMT/HE (Li et al. 2018; Luo et al. 2020; Song et al. 2022), Fermi/LAT and Fermi/GBM at 10:19:08 on 2019 May 30 (UT dates are adopted). Insight-HXMT/HE detected GRB 190530A with  $T_{90} = 20.31$  s in the 80–800 keV energy band (Yi et al. 2019), the location is (R.A., decl.) = (120.53, 35.47) degrees (J2000) with an error radius of 1 degree. The burst was especially bright in the Insight-HXMT/HE detector, producing over 18,182 counts. The count rate above the background in the most illuminated HE detectors and the total count from this burst are 214,189 (Yi et al. 2019). The  $T_{90}$  of GRB 190530A is 18.4 s in Fermi/GBM detection, and the onboard location is (R.A., Dec) = (120.7, 36.1) degrees (J2000) with an error radius of  $1^\circ$  (Biltzinger et al. 2019). The discrepancy of the detected duration ( $T_{90}$ ) is caused by the difference in sensitivity of Insight-HXMT/HE and Fermi/GBM in their different energy bands. The gamma-ray fluence and the one-second peak photon flux in the 10–1000 keV band are  $S_\gamma = (3.72 \pm 0.01) \times 10^{-4}$  erg cm $^{-2}$  and  $F_\gamma = 160.5 \pm 0.7$  photon s $^{-1}$  cm $^{-2}$  with Fermi/GBM (Bissaldi & Meegan 2019). Fermi/LAT detected this burst, and the onboard location is (R.A., decl.) = (120.76, 35.5) degrees (J2000) with an error radius of 0.12 degree (Longo et al. 2019).

### 2.2. Optical and X-Ray Afterglow Observations

GWAC-N is adjusted to simultaneously observe with Insight-HXMT/HE, which can perform cross-identification of the follow-up observations of X/ $\gamma$ -ray and optical transients. The GRB 190530A was jointly observed by Insight-HXMT/HE and GWAC-N. The Swift/XRT detected the X-ray afterglow of the burst and published the observation in GCN Circulars at 04:14:12 on 2019 May 31 (Melandri et al. 2019). GWAC-N is currently located at the Xinglong Observatory (lat =  $40^\circ 23' 39''$  N, lon =  $117^\circ 34' 30''$  E) in China, part of the future ground segment of the space-based multi-band astronomical variable objects monitor (SVOM) mission dedicated to the study of the transient sky with both space-based and ground-based multi-wavelength instruments (Wei et al. 2016). Due to the extremely large field of view (FOV) ( $25^\circ \times 25^\circ$ ) of GWAC array, with fast follow-up GWAC-F60 (the 60 cm telescope of GWAC) and GWAC-F30 (the 30 cm telescope of GWAC) telescopes and the fast responding observation system (the AOM presented in Han et al. 2021), the GWAC-N is well suited for the optical follow-up of GRB candidates detected by GWAC array with a localization accuracy of 1 arc second for the target source (Turpin et al. 2020). For the candidates, fast extra multi-wavelength follow-up observations at deeper magnitudes (typically  $R \sim 19$  for an exposure of 120 s). These provide multiple observing capabilities and strategies for the optical tracking of gravitational waves (GWs) and GRBs.

As the time of Insight-HXMT/HE trigger was before sunset at Xinglong Observatory, GWAC array was not involved in the observation. We observed the optical emission of GRB 190530A, using GWAC-F30 to search and locate its position at 2.49 h after the burst, and published the observation in GCN Circulars at 01:42:46 on 2019 May 31. We began imaging the field using GWAC-F30, which uses different filters (Johnson *UBVRI*) with a large FOV and obtained seven images of 20 s exposures. The search location result of GRB 190530A is shown in Figure 1. The purple color in the left figure is the location of Insight-HXMT/HE with an error of  $1^\circ$ . The red and green colors are the location from Fermi/LAT with an error of  $0^\circ.12$  and Fermi/GBM with an error of  $1^\circ$ , respectively. The blue circle in the figure represents the position of GRB 190530A. The point-spread-function photometry is applied using the DAOPHOT package (Stetson 1987) from the IDL Astronomy User's Library.<sup>6</sup> Data reduction is carried out following the standard routines using the IRAF<sup>7</sup> package, and the photometry is  $R = 15.10 \pm 0.04$  mag (Xin et al. 2019a) reported in Table 1. The photometry is based on the nearby USNO-B1.0 stars. Subsequently, we made a deep follow-up observation of GRB 190530A detected by GWAC-F30 with the 2.16 m telescope equipped with the BFOSC camera at

<sup>6</sup> <http://idlastro.gsfc.nasa.gov/>

<sup>7</sup> <http://ast.noao.edu/data/software/>

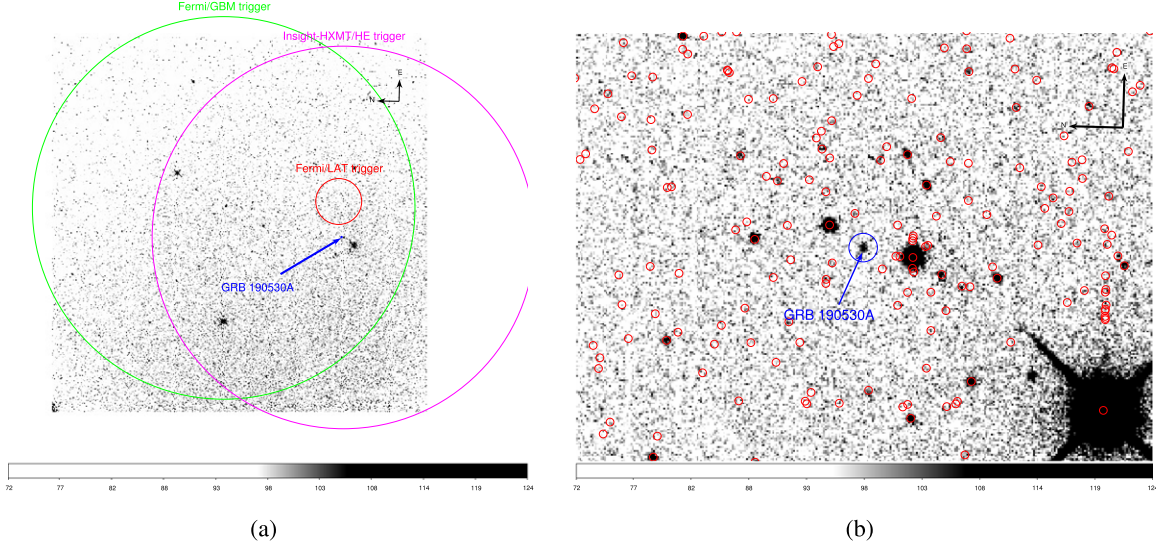


**Figure 1.** The observed field near GRB 190 530A in the  $R$  filter with GWAC-F30. (a) The position of GRB 190 530A from Insight-HXMT/HE, with an error of 1 degree (purple color). The red and green colors are the location from Fermi/LAT with an error of 0.12 degree and Fermi/GBM with an error of 1 degree, respectively. (b) The blue circle in the image represents the position of GRB 190 530A.

**Table 1**  
Optical Observation of GRB 190 530A

$T - T_0$ (s) <sup>a</sup>	Exposure (s)	Mag <sup>b</sup>	$\sigma$ <sup>c</sup>	Filter	Telescope <sup>d</sup>
8964	$7 \times 20$	15.10	0.04	$R$	GWAC-F30
96768	$62 \times 50$	19.63	0.10	$R$	Xinglong-2.16m
114196	$19 \times 60$	18.50	0.10	$R$	AbAO <sup>(1)</sup>
116899	900	19.39	0.05	$R$	SAO RAS <sup>(2)</sup>
193223	$29 \times 60$	19.62	0.07	$R$	Mondy and AbAO <sup>(3)</sup>
200248	$30 \times 60$	19.70	0.14	$R$	Mondy and AbAO <sup>(3)</sup>
275616	900	21.30	0.30	$R$	HCT <sup>(4)</sup>
37784	...	17.63	0.10	$Rc$	OSN <sup>(5)</sup>
124856	$7 \times 120$	19.51	0.04	$Rc$	OSN <sup>(6)</sup>

**Notes.**

<sup>a</sup>  $T - T_0$  is the midpoint of each observation.

<sup>b</sup> Not taking into account the Galactic extinction.

<sup>c</sup>  $\sigma$  is the uncertainty in the magnitude. Here we present the statistic uncertainty only.

<sup>d</sup> (1) Belkin et al. (2019); (2) Moskvitin & Uklein (2019); (3) Belkin & IKI GRB FuN Collaboration (2019) (4) Kumar & Pandey (2019); (5) Kann et al. (2019a); (6) Kann (2019).

Xinglong Observatory. 62 images of 50 s exposures were obtained. The optical afterglow was clearly detected in our stacked image with a magnitude of  $R = 19.63 \pm 0.10$  mag (Xin et al. 2019b) at the mid time of about 1.12 days after the burst, calibrated with nearby SDSS stars. The redshift  $z$  of GRB 190 530A was set to 0.9386 (Gupta et al. 2022). Note that we denote  $T_0$  as the burst trigger time of the initial detection.

The bright optical counterpart of GRB 190 530A was also detected by several ground-based telescopes, such as the AS-32

(0.7 m) telescope at the Abastumani Observatory at  $\sim 1.32$  days (Belkin et al. 2019; Belkin & IKI GRB FuN Collaboration 2019), the 1.5 m telescope at the Sierra Nevada Observatory in Spain at  $\sim 0.44$  days (Kann et al. 2019a, 2019b), the 1 m telescope of SAO RAS at  $\sim 1.35$  days (Moskvitin & Uklein 2019), the AZT-33IK telescope at the Sayan Observatory at  $\sim 2.23$  days (Belkin & IKI GRB FuN Collaboration 2019), and the 2 m Himalayan Chandra Telescope at the Indian Astronomical Observatory at  $\sim 3.19$  days

(Kumar & Pandey 2019). The X-ray Telescope (XRT; Burrows et al. 2005) onboard Swift began observing the field of GRB 190530A, 33.8 ks after the burst trigger (Melandri et al. 2019).

### 3. Spectral Analysis of the Prompt Emission

#### 3.1. Selected Data and Spectral Analysis

We obtain all events data in 18 CsI detectors from the Insight-HXMT/HE trigger catalog.<sup>8</sup> The source time intervals for all detectors are chosen to be the same as for the GRB data analysis, thus data of all detectors can be added up to reduce the statistical uncertainties. We study the temporal and spectral prompt emission properties of GRB 190530A using the five brightest HE detectors (CsI 0, 2, 4, 6 and 10) with the largest effective areas. We use the Insight-HXMT burst analysis (*HXMTbeta*) software to create prompt emission light curves and spectra using Insight-HXMT/HE observation. The background signals are estimated from the segments before and after the GRB for the time intervals  $T_0 - 300$  s to  $T_0 - 50$  s and  $T_0 + 70$  s to  $T_0 + 300$  s, respectively.

Meanwhile, we use *gtburst* software to obtain Fermi/GBM data in time-stamped event (TTE) mode from the Fermi/GBM trigger catalog.<sup>9</sup> We select the brightest NaI detectors (NaI 1 and 2) and BGO detector (BGO 0) as these detectors are closer to the direction of the burst. We use the *gtburst* software to create prompt emission light curves and spectra using Fermi/GBM observation. The background signal is estimated for the same time interval as for the Insight-HXMT/HE data.

We perform the modeling of the joint Insight-HXMT/HE and Fermi/GBM spectrum using the Heasoft tool *grppha* (Virgili et al. 2012) software to investigate the possible emission mechanisms of GRB 190530A. We employ the typical empirical Band function (Band et al. 1993) to fit spectral data of GRB 190530A. The Band function is described as a smoothly broken power law:

$$N_{\text{Band}}(E) = \begin{cases} A \left( \frac{E}{100\text{keV}} \right)^\alpha \exp\left(-\frac{E}{E_0}\right), & E < (\alpha - \beta)E_0 \\ A \left[ \frac{(\alpha - \beta)E_0}{100\text{keV}} \right]^{\alpha - \beta} \exp(\alpha - \beta) \left( \frac{E}{100\text{keV}} \right)^\beta, & E \geq (\alpha - \beta)E_0 \end{cases} \quad (1)$$

where  $A$  is the normalization of Band spectrum,  $\alpha$  and  $\beta$  are the low-energy and high-energy photon spectral indices,  $E_0$  is break energy of the spectrum. The peak energy in the spectrum is called  $E_p$ , which is related to  $E_0$  by  $E_p = (2 + \alpha)E_0$ . As the obtained spectral files for Insight-HXMT/HE and Fermi/GBM are consistent with statistics for Poisson fluctuations with Gaussian background (*pgstat*), the  $\chi^2$ -statistics is used for the joint spectral analyses. The spectral fitting package *Xspec*

(Arnaud 1996) is used for the spectral analysis. We consider Insight-HXMT/HE and Fermi/GBM spectrum over the energy range of 8–900 keV (NaI detectors), 0.2–40 MeV (BGO detectors) and 100–600 keV (HE detectors) for the spectral analysis.

#### 3.2. Analysis Results

##### 3.2.1. The Main Prompt Emission

The  $\gamma$ -ray emission light curve of GRB 190530A consists of a precursor emission (Episode I,  $T_0 - 0.3$  s to  $T_0 + 4.5$  s) and main prompt emission ( $T_0 + 7.8$  s to  $T_0 + 24.4$  s), as shown Figure 2. The main prompt emission consists of three pulses, e.g., Episode II ( $T_0 + 7.8$  s to  $T_0 + 11.5$  s), III ( $T_0 + 11.5$  s to  $T_0 + 16.1$  s) and IV ( $T_0 + 16.1$  s to  $T_0 + 24.4$  s). The background-subtracted 0.064 s binned light curves of Insight-HXMT/HE and Fermi/GBM detectors are provided in multiple energy channels (given in the ten panels) in Figure 2. The fitting result of time-integrated spectrum (from  $T_0 - 0.3$  s to  $T_0 + 24.4$  s) for GRB 190530A is shown in Figure 3, with  $\alpha = -1.00 \pm 0.01$ ,  $\beta = -3.60 \pm 0.13$ , and  $E_p = 883.5 \pm 11.6$  keV. Then we subdivide the prompt emission light curve of GRB 190530A into 13 intervals after considering the temporal characteristics, as shown in Figure 2. The fitting results of time-resolved spectrum is show in Table 2. The time-integrated and time-resolved spectrum fitting results shown that the Band model can well describe the spectral shape for all time intervals. Given the sensitivity of the detectors, the remaining high-energy bump indicates that there might not exist an additional high-energy component.

Because the prompt emission light curve of GRB 190530A exhibits multi-pulse behavior, the spectral evolution may be influenced by a complex central engine. The temporal evolution of  $E_p$  and  $\alpha$  for GRB 190530A display significant “double-tracking” trends along with photon counts, as shown in Figure 4. It is a multiple-pulse burst rather than a single-pulse burst like for GRB 131231A in Li et al. (2019), which also has the “double-tracking” pattern for both its  $E_p$  and  $\alpha$  in all time-resolved spectra. In general, multiple-pulse bursts are more difficult to extrapolate for the evolution of  $E_p$  and  $\alpha$ . In Uhm et al. (2018) and Gupta et al. (2022), the “double-tracking” behavior was interpreted using the synchrotron radiation model. Zhang & Mészáros (2002) presented the  $E_p \propto L^{1/2}$  relation in the synchrotron model, where  $L$  is the luminosity of the ejecta. Regarding the prompt spectral evolutions, the synchrotron emission origin can account for the “double-tracking” behaviors of  $E_p$  and  $\alpha$ .

##### 3.2.2. The Precursor Emission

Some GRBs light curves consist of a weak segment followed by a bright-burst segment. The weak segment is called precursor emission, which may be separated or tightly

<sup>8</sup> <http://archive.hxmt.cn/grb>

<sup>9</sup> <https://heasarc.gsfc.nasa.gov/W3Browse/fermi/fermigtrig.html>

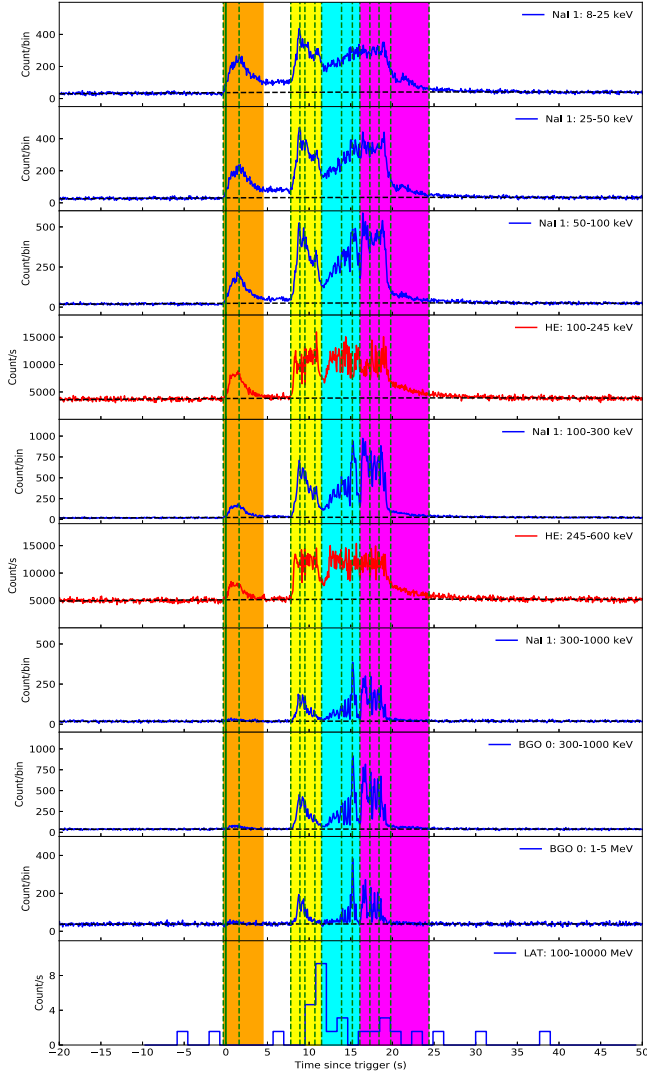


**Figure 2.** The prompt emission light curves of GRB 190530A with 0.064 s binned. Observations from the Insight-HXMT/HE detectors and Fermi detectors are shown in red solid and blue solid lines, respectively. The green vertical solid line represents the burst trigger time and green vertical dotted lines correspond to the time ranges used for spectral analysis. The time interval from  $T_0 - 0.3$  s to  $T_0 + 24.4$  s is subdivided into 13 intervals after considering the temporal characteristics. Episode I:  $T_0 + (-0.3-4.5)$  s, Episode II:  $T_0 + (7.8-11.5)$  s, Episode III:  $T_0 + (11.5-16.1)$  s and Episode IV:  $T_0 + (16.1-24.4)$  s.

connected to the subsequent main structure (main prompt emission). These weak precursors may or may not trigger a gamma-ray burst. GRB 190530A showed a precursor emission in its light curve, i.e., Episode I, as shown in Figure 2. The spectral indices of the precursor are essentially the same as that of the main prompt emission in Table 2, and both show the same “double-tracking” pattern of  $E_p$  and  $\alpha$  as the main prompt emission in Figure 4. It indicates that they have the same physical origin.

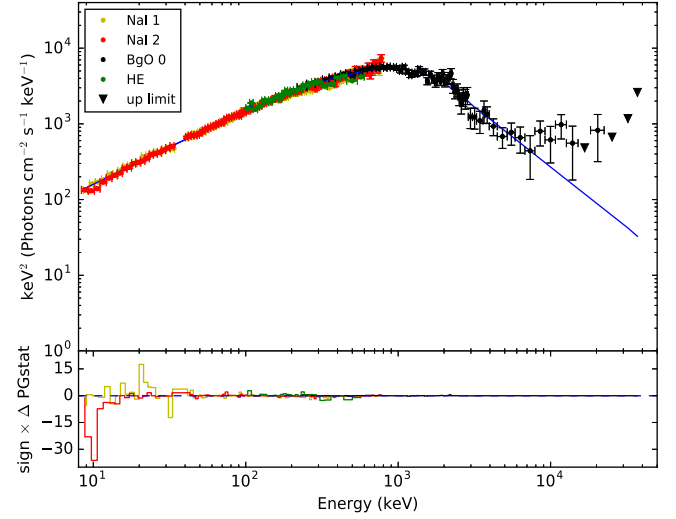


**Figure 3.** Joint fit of Insight-HXMT/HE and Fermi/GBM time-integrated ( $T_0 - 0.3$  s to  $T_0 + 24.4$  s) spectrum with band function.

### 3.2.3. The Spectral Lag

The spectral lag of a GRB is defined as the time delay of high-energy photons with respect to low-energy photons, and is commonly observed in long GRBs (Norris et al. 1986; Cheng et al. 1995; Band 1997; Norris et al. 2000). To study GRB spectral lag, which can be measured as a relative lag of the light curves in different energy bands, the cross correlation function analysis is used. For GRB 190530A, the spectral lag ( $\tau$ ) with respect to 100–245 keV is estimated for the 245–600 keV energy band of the Insight-HXMT/HE detectors of GRB 190530A. Furthermore, the spectral lag ( $\tau$ ) with respect to 8–25 keV is estimated for four energy bands (8–25, 25–50, 50–100, 100–300, and 300–1000 keV) of the NaI detectors and two energy bands (300–1000 and 1000–5000 keV) of the BGO detectors. The procedure to obtain the spectral lag  $\tau$  can be seen in Lu et al. (2018). As shown in Figure 5, the results of GRB 190530A show that  $\tau$  increases with increasing energy  $E$  (given the same reference band for the same detector). It shows a clear dependence of  $\tau$  on  $E$ , with a linear function  $\tau = k_\tau \log(E) + b = (0.17 \pm 0.03) \log E - 3.0 \pm 0.06$ . A similar dependence of  $\tau$  on  $E$  can be also found in the H2S-dominated tracking pulses (Lu et al. 2018). This may indicate that the spectral lag is the result of the temporal evolution of  $E_p$  (Ukwatta et al. 2012). The generic physical model discussed by Uhm & Zhang (2016) and Uhm et al. (2018) suggests that this relation can be realized more easily if the emission originates from electrons within the same fluid unit, so that the emission features can evolve continuously as the fluid unit moves in space (Lu et al. 2018). Such a scenario naturally produces asymmetric pulse profiles. Lu et al. (2018) found that the spectrum evolves uniformly within each pulse, which indicates that pulses are the fundamental units of GRB radiation.

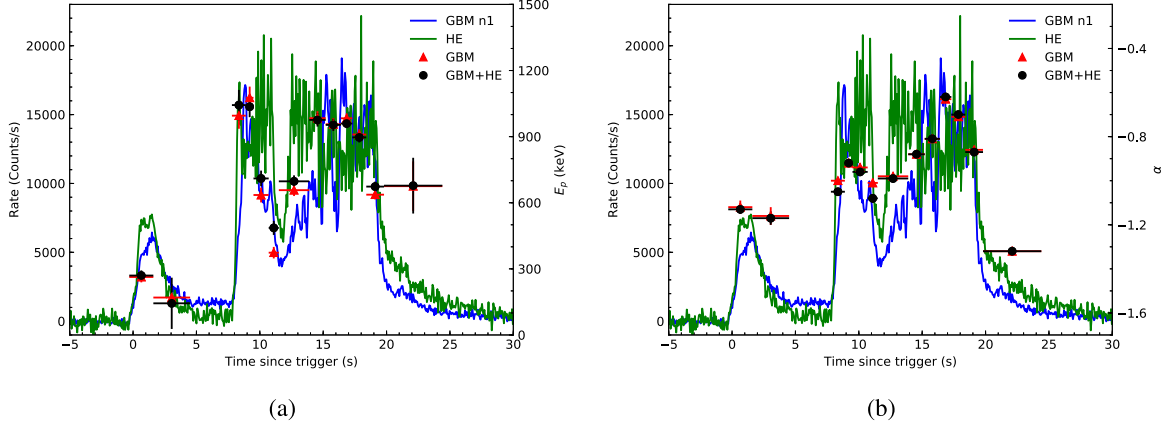


**Figure 4.** The evolution of  $E_p$  (right Y-axis in (a)) and  $\alpha$  (right Y-axis in (b)) as the photon counts (left Y-axis).

**Table 2**  
Spectral Fitting Results of GRB 190 530A with Insight-HXMT/HE and Fermi/GBM Data

Interval (s)	$\alpha$	$\beta$	$E_p$ (keV)	Flux ( $\text{erg s}^{-1} \text{cm}^{-2}$ )	$E_{\gamma,\text{iso}}$ (erg)	$L_{p,\text{iso}}$ ( $\text{erg s}^{-1}$ )	$\chi^2/\text{dof}$
-0.3–24.4	$-1.00 \pm 0.01$	$-3.60 \pm 0.13$	$883.5 \pm 11.6$	$2.43 \pm 0.02 \times 10^{-5}$	$1.43 \pm 0.01 \times 10^{54}$	$2.17 \pm 0.02 \times 10^{53}$	845/594
Episode I							
-0.3–4.5	$-1.17 \pm 0.02$	$-2.46 \pm 0.10$	$197.2 \pm 19.4$	$3.72 \pm 0.23 \times 10^{-6}$	$8.64 \pm 0.01 \times 10^{52}$	$5.81 \pm 0.37 \times 10^{52}$	499/454
-0.3–1.6	$-1.13 \pm 0.02$	$-2.52 \pm 0.17$	$269.6 \pm 23.4$	$6.93 \pm 0.69 \times 10^{-6}$	...	...	471/462
1.6–4.5	$-1.17 \pm 0.03$	$-2.53 \pm 0.14$	$143.6 \pm 16.3$	$3.82 \pm 0.29 \times 10^{-6}$	...	...	415/446
Episode II							
7.8–11.5	$-1.00 \pm 0.01$	$-2.59 \pm 0.05$	$807.3 \pm 31.6$	$4.17 \pm 0.09 \times 10^{-5}$	$3.28 \pm 0.07 \times 10^{53}$	$3.33 \pm 0.07 \times 10^{53}$	740/600
7.8–8.9	$-1.05 \pm 0.01$	$-2.33 \pm 0.08$	$1043.2 \pm 68.8$	$4.26 \pm 0.47 \times 10^{-5}$	...	...	660/600
8.9–9.5	$-0.92 \pm 0.01$	$-2.90 \pm 0.13$	$1035.7 \pm 47.4$	$7.51 \pm 0.28 \times 10^{-5}$	...	...	510/600
9.5–10.7	$-0.96 \pm 0.01$	$-2.79 \pm 0.14$	$710.2 \pm 35.6$	$4.09 \pm 0.15 \times 10^{-5}$	...	...	558/600
10.7–11.5	$-1.08 \pm 0.02$	$-2.40 \pm 0.10$	$485.9 \pm 31.9$	$2.35 \pm 0.14 \times 10^{-5}$	...	...	657/549
Episode III							
11.5–16.1	$-0.91 \pm 0.01$	$-3.91 \pm 0.26$	$865.9 \pm 25.5$	$3.75 \pm 0.05 \times 10^{-5}$	$4.14 \pm 0.05 \times 10^{53}$	$2.79 \pm 0.05 \times 10^{53}$	776/600
11.5–13.9	$-0.99 \pm 0.01$	$-3.66 \pm 0.46$	$697.2 \pm 27.1$	$2.07 \pm 0.07 \times 10^{-5}$	...	...	600/600
13.9–15.2	$-0.88 \pm 0.01$	$-4.06 \pm 0.46$	$975.9 \pm 30.4$	$5.21 \pm 0.11 \times 10^{-5}$	...	...	622/600
15.2–16.1	$-0.81 \pm 0.01$	$-4.13 \pm 0.43$	$953.3 \pm 27.7$	$6.26 \pm 0.12 \times 10^{-5}$	...	...	563/600
Episode IV							
16.1–24.4	$-0.85 \pm 0.01$	$-5.27 \pm 1.09$	$924.3 \pm 23.2$	$3.06 \pm 0.49 \times 10^{-5}$	$6.17 \pm 0.10 \times 10^{53}$	$5.88 \pm 0.13 \times 10^{53}$	776/600
16.1–17.3	$-0.62 \pm 0.01$	$-6.90 \pm 2.36$	$959.6 \pm 21.1$	$9.50 \pm 0.05 \times 10^{-5}$	...	...	647/600
17.3–18.4	$-0.70 \pm 0.01$	$-4.25 \pm 0.41$	$896.5 \pm 23.0$	$7.59 \pm 0.13 \times 10^{-5}$	...	...	587/600
18.4–19.8	$-0.87 \pm 0.01$	$-3.73 \pm 0.39$	$673.3 \pm 22.4$	$3.53 \pm 0.09 \times 10^{-5}$	...	...	686/600
19.8–24.4	$-1.32 \pm 0.02$	$-1.95 \pm 0.08$	$677.5 \pm 126.5$	$7.57 \pm 0.46 \times 10^{-6}$	...	...	678/600

### 3.2.4. Correlations

Two experimental correlations are tested, i.e., the  $E_{p,z} - E_{\gamma,\text{iso}}$  (Amati; Amati et al. 2002; Amati 2006) and  $E_{p,z} - L_{p,\text{iso}}$  (Yonetoku; Yonetoku et al. 2004, 2010) relations. Wang et al. (2018) investigated several empirical correlations

(Amati, Frail, Ghirlanda, and Liang-Zhang), and they suggest the  $E_{p,z} - E_{\gamma,\text{iso}}$  (Amati) correlation as

$$\frac{E_{p,z}}{100 \text{ keV}} = (0.63 \pm 0.31) \left( \frac{E_{\gamma,\text{iso}}}{10^{52} \text{ erg}} \right)^{0.69 \pm 0.07}, \quad (2)$$

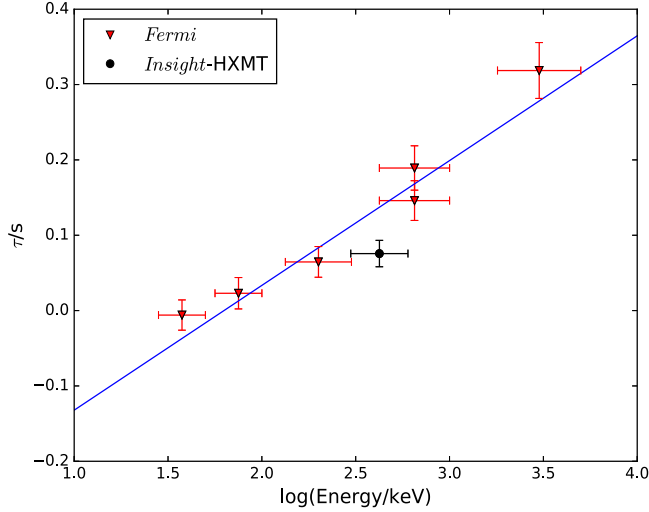


**Figure 5.** GRB 190 530A spectral lag  $\tau$  evolves with energy  $E$ . The blue solid line represents the best linear fitting result for its spectral lag behavior.

where  $E_{p,z} = (1+z)E_p$  is the peak energy in the rest frame. The isotropic gamma-ray energy  $E_{\gamma,iso}$  of a GRB is calculated as  $E_{\gamma,iso} = \frac{4\pi D_L^2 S_\gamma k}{1+z}$ , where  $S_\gamma$  is the gamma-ray fluence in the instrument band,  $D_L$  is the luminosity distance of the source at the redshift  $z$ , and the parameter  $k$  is a factor to convert the observed gamma-ray energy in a given bandpass into a broad band (e.g., 1–10<sup>4</sup> keV in the rest frame) with the observed GRB spectrum. The  $E_{p,z} - L_{p,iso}$  (Yonetoku) correlation as (Yonetoku et al. 2004, 2010)

$$\frac{L_{p,iso}}{10^{52} \text{ erg s}^{-1}} = (2.34^{+2.29}_{-1.76}) \left( \frac{E_{p,z}}{1 \text{ keV}} \right)^{2.0 \pm 0.2}, \quad (3)$$

where  $L_{p,iso} = (1+z)L_p$  is the one-second peak luminosity in the rest frame. The peak luminosity with the proper  $k$ -correction can be calculated as  $L = 4\pi d_L^2 F_\gamma k_c$  (Yonetoku et al. 2004), where  $d_L$  and  $F_\gamma$  are the luminosity distance and observed peak flux integrated between 30 and 10,000 keV, respectively. The  $k$ -correction factors ( $k_c$ ) are estimated via the same method used by Amati et al. (2002). GRB 190 530A satisfies the Amati (as shown in Figure 6) and Yonetoku (as shown in Figure 7) relations and the same relations are obtained from Gupta et al. (2022).

#### 4. Optical and X-Ray Afterglow

The GRB 190 530A data are available on the Swift online repository<sup>10</sup> hosted by the University of Leicester (Evans et al. 2009, 2010). To understand the origin of the X-ray and optical afterglow data, we produce the spectral energy distribution using joint optical and X-ray data. We perform the joint optical

<sup>10</sup> [https://www.swift.ac.uk/xrt\\_curves/00020893/](https://www.swift.ac.uk/xrt_curves/00020893/)

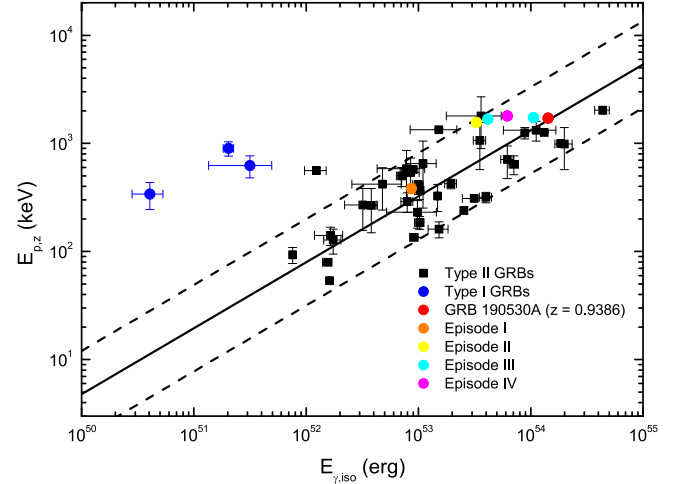


**Figure 6.** GRB 190 530A in  $E_{p,z} - E_{\gamma,iso}$  plane (Amati relation). The data points in the graph are taken from Wang et al. (2018). Red circle, orange circle, yellow circle, cyan circle and magenta circle represent all pulses, Episode I, Episode II, Episode III and Episode IV, respectively. The solid line mean the Amati relation, and their  $2\sigma$  dispersion regions are shown with the dashed lines.

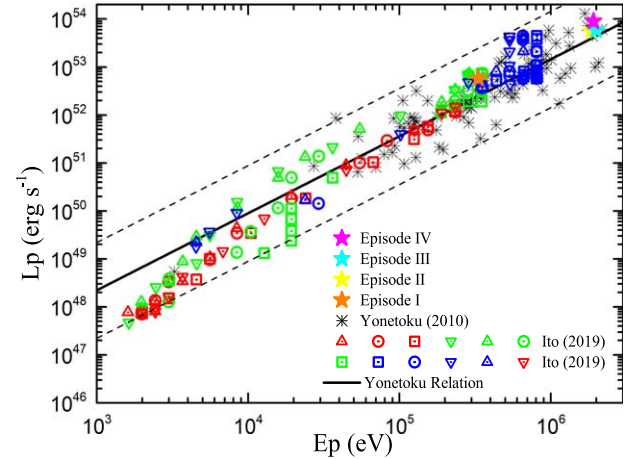


**Figure 7.** GRB 190 530A in  $E_{p,z} - L_{p,iso}$  plane (Yonetoku relation). Orange pentagram, yellow pentagram, cyan pentagram and magenta pentagram represent Episode I, Episode II, Episode III and Episode IV, respectively. The data points in the graph are taken from Ito et al. (2019) and Yonetoku et al. (2010). The solid line represents the Yonetoku relation, and the dashed line means the  $2\sigma$  confidence interval of Yonetoku relation.

and X-ray data modeling using *Xspec* (Arnaud 1996) software. We include the Galactic and intrinsic absorber using the *Xspec* models *phabs* and *zphabs*. The absorption of the Galaxy with  $N_H = 5.07 \times 10^{20} \text{ cm}^{-2}$  is adequate to address the observed soft X-ray absorption (Willingale et al. 2013). For the extinction at the redshift of the burst, the optical extinction is found to be negligible even when the extinction laws of the Galaxy and the Small and Large Magellanic Clouds are used in the fit. The spectrum can be well fitted by a power-law with

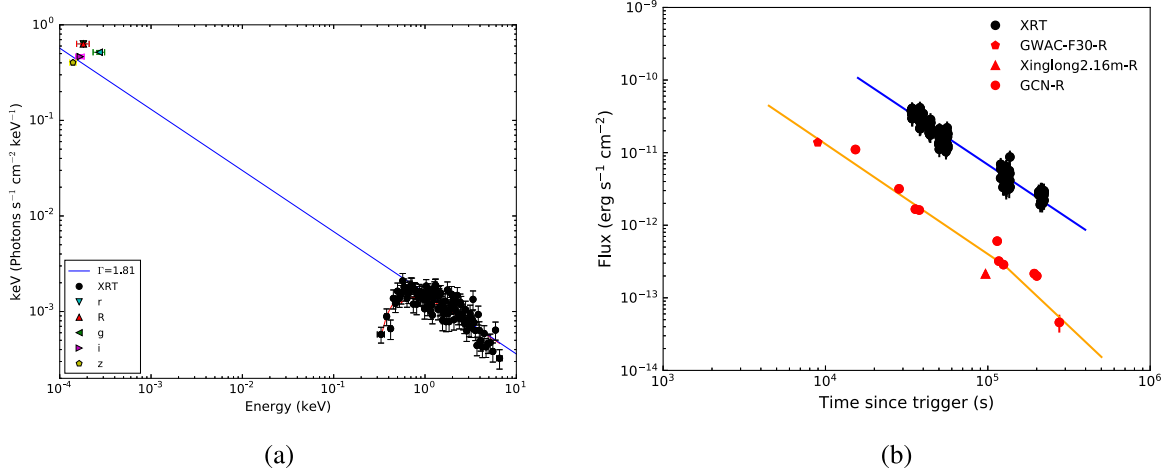


**Figure 8.** The temporal and spectral analysis of GRB 190530A. (a): SED analysis of GRB 190530A, the blue line shows the extrapolation for the spectral index of X-ray emission. (b) The temporal fitting of GRB 190530A. The fitting results of the X-ray and optical afterglow are represented with a single power-law (blue line) and a broken power-law (orange line), respectively.

$\Gamma_{\text{OX}} = 1.81 \pm 0.14$  and  $\chi^2/\text{dof} = 478/499$  (as shown in Figure 8), where dof stands for degrees of freedom.

To get the temporal profile of the GRB 190530A afterglow, we employ a single power-law function

$$F = F_0 t^{-\alpha}, \quad (4)$$

where  $F_0$  is the flux normalization and  $\alpha$  is the afterglow flux decay index, and also a broken power-law function

$$F = F_1 \left[ \left( \frac{t}{t_b} \right)^{\omega\alpha_1} + \left( \frac{t}{t_b} \right)^{\omega\alpha_2} \right]^{-1/\omega}, \quad (5)$$

where  $F_1$  is the flux normalization,  $\alpha_1$  and  $\alpha_2$  are respectively the afterglow flux decay indices before and after the break time ( $t_b$ ), and  $\omega$  is a smoothness parameter which represents the sharpness of the break.

For the  $R$ -band afterglow, we first obtain the data which are corrected for the Galactic extinction in the direction of the burst using the model described in Schlafly & Finkbeiner (2011). The  $R$ -band light curve can be well fitted by a broken power law with a normal decay index of  $\alpha_{\text{R,I}} = 1.50 \pm 0.08$ , and a break at  $t_b \approx 120$  ks followed with a steep index  $\alpha_{\text{R,II}} = 2.04 \pm 0.11$ , as shown in Figure 8 (b). Swift/XRT did not explicitly detect the phenomenon of a jet break, the X-ray afterglow can be fitted using a single power-law function with a temporal decay index of  $\alpha_{\text{X}} = 1.49 \pm 0.07$ .

Combining the results of our temporal analysis and spectral analysis, we use the closure relation ( $\alpha - \beta$ ,  $\beta$  and  $\alpha$  are the spectral index and temporal decay index, respectively) of the fireball external forward shock model to test the optical and X-ray data of GRB 190530A. The value of spectral index is  $\beta_{\text{OX}} = \Gamma_{\text{OX}} - 1 = 0.81 \pm 0.14$ . We find that the temporal slopes of the first segment for both optical and X-ray bands ( $\alpha_{\text{R,I}} = 1.50 \pm 0.08$ ,  $\alpha_{\text{X}} = 1.49 \pm 0.07$ ) satisfy the relation

$\alpha = 3\beta/2 \sim 1.22 \pm 0.21$  for the normal decay in ISM circumburst medium in a slow-cooling spectral regime ( $\nu_m < \nu_o < \nu_X < \nu_c$  ( $\nu_m$  is the characteristic synchrotron frequency,  $\nu_c$  is the cooling frequency,  $\nu_o$  and  $\nu_X$  is the frequency of optical and X-ray bands). For the post break of the optical band, it also satisfy corresponding post jet break closure relation  $\alpha = (6\beta + 3)/4 \sim 1.97$ . The  $p$  value of GRB 190530A is estimated to be  $p = 2\beta + 1 = 2.62 \pm 0.28$ .

To model the observed data (X-ray and optical data), we consider standard external forward shock in ISM circumburst medium without energy injection, with the following free parameters, i.e.,  $\Gamma_0$  (the initial Lorentz factor),  $p$ ,  $n_0$  (the medium density),  $E_{\text{K,iso}}$  (the isotropic kinetic energy),  $\epsilon_e$  (the fraction of the shock energy in radiating electrons),  $\epsilon_b$  (the fraction of the shock energy in magnetic fields),  $\theta_j$  (the jet opening angle). The Monte Carlo method is utilized to model the best parameters. The best fitting parameters and their probability distribution are shown in Figure 9. The best-fitting parameters ( $1\sigma$  confidence level) of the external forward shock model are  $\log \Gamma_0 = 2.84^{+0.30}_{-0.42}$ ,  $p = 2.60^{+0.26}_{-0.23}$ ,  $\log n_0 = 0.76^{+0.86}_{-1.15}$ ,  $\log E_{\text{K,iso}} = 55.57^{+0.78}_{-0.67}$ ,  $\log \epsilon_e = -1.03^{+0.43}_{-0.49}$ ,  $\log \epsilon_b = -6.97^{+0.65}_{-0.84}$ ,  $\theta_j = 3.81^{+0.71}_{-0.87}$ , respectively.

## 5. Discussion and Conclusions

GRB 190530A was jointly observed by Insight-HXMT/HE and GWAC-N with their extremely large FOV. After triggered by Insight-HXMT/HE and Fermi/GBM, we observed the optical emission of GRB 190530A, using GWAC-F30 to search and locate its position. Subsequent observation of the late afterglow of GRB 190530A was made with the 2.16 m telescope at Xinglong Observatory. GRB 190530A was also

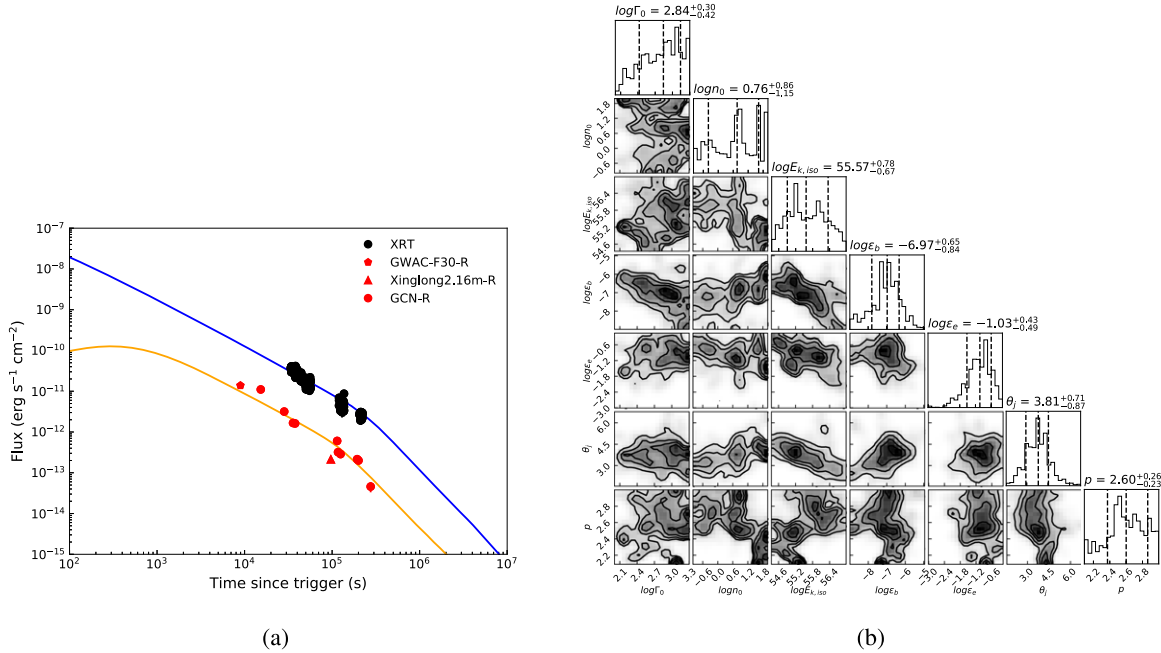


**Figure 9.** Modeling the optical and X-ray light curves with an external forward shock model in ISM circumburst medium. (a) The theoretical prediction from the external forward shock, compared with the observed data. (b) The best fitting parameters and their probability distribution.

observed by Fermi/GBM, Swift/XRT and other ground-based optical telescopes.

We studied the temporal and spectral characteristics of the prompt emission of GRB 190530A using Insight-HXMT/HE and Fermi/GBM observations. An analysis of this event in the afterglow was carried out using GWAC-F30, the 2.16 m telescope at Xinglong Observatory, Swift/XRT and other optical observations. We found that from the precursor, prompt emission to afterglow of GRB 190530A all emission can be interpreted with synchrotron radiation. The properties of GRB 190530A are summarized as follows:

1. In the prompt emission of GRB 190530A, a single Band function without adding extra components is adequate to fit the Insight-HXMT/HE and Fermi/GBM data for the time-integrated and time-resolved spectra. The spectrum shows the “double-tracking” evolution pattern both for  $E_p$  and  $\alpha$ ; the spectral lag increases with increasing photon energy,  $\tau = -3.0 \pm 0.06 + (0.17 \pm 0.03)\log E$ ; GRB 190530A well satisfies the Amati and Yonetoku relations. The prompt emission of GRB 190530A originated from synchrotron radiation.
2. The spectral index of the precursor radiation is essentially the same as that of the main prompt emission, and both  $E_p$  and  $\alpha$  show the same “double-tracking” pattern as the main prompt emission. These suggest that the precursor, despite being a pre-burst and weaker, may have the same

origin as the main prompt emission, and both of which may be produced by synchrotron radiation.

3. The afterglow in the X-ray and optical bands could be well explained with the external forward shock model in ISM circumburst medium. The best fitting parameters of the external forward shock model are  $\log \Gamma_0 = 2.84^{+0.30}_{-0.42}$ ,  $p = 2.60^{+0.26}_{-0.23}$ ,  $\log n_0 = 0.76^{+0.86}_{-1.15}$ ,  $\log E_{k,iso} = 55.57^{+0.78}_{-0.67}$ ,  $\log \epsilon_e = -1.03^{+0.43}_{-0.49}$ ,  $\log \epsilon_b = -6.97^{+0.65}_{-0.84}$ ,  $\theta_j = 3.81^{+0.71}_{-0.87}$ , respectively.

A precursor is generally defined as an emission episode whose peak intensity is much lower than that of the main prompt emission episode and with a quiescent separation period from the main prompt emission episode (Koshut et al. 1995; Burlon et al. 2008, 2009; Troja et al. 2010). Precursors may or may not trigger the gamma-ray detectors (Lazzati 2005), e.g., GRB 041219A (Götz et al. 2011), GRB 050820A (Cenko et al. 2006), and GRB 060124 (Romano et al. 2006). For GRB 190530A, there is a quiet period of about 3 seconds between the precursor emission and the main prompt emission. The precursor of GRB 190530A has triggered the gamma-ray detectors, may be due to that GRB 190530A is bright enough. Two leading models have been advocated to interpret the precursor. One is that the collapse of a rapidly rotating stellar core leads to fragmentation (King et al. 2005). If the delayed accretion of fragmented debris leads a second burst, the debris must have comparable masses with the materials in the initial

major accretion. This behavior has not been seen to date in numerical simulations (e.g., Masada et al. 2007; Metzger et al. 2008). Another is that there is a long-standing speculation when rotation and magnetic fields are taken into account, the core collapse of massive star can lead to some form of magnetohydrodynamics (MHD) outflows (Wang & Mészáros 2007). In that scenario, the precursor is produced by a weak jet formed during the initial core collapse, possibly related to MHD processes associated with a short-lived massive star, while the main prompt emission is produced by a stronger jet fed by the fallback accretion onto the black hole, resulted from the collapse of massive star. For GRB 190530A, it is still hard to conclude which model is preferred.

Two main types of objects are thought to power the central engine: a stellar-mass black hole, and a rapidly spinning, highly magnetized magnetar. Li et al. (2018) studied the X-ray light curves sample of 101 bursts with a plateau phase and measured redshift. They found only 20% of GRBs were consistent with having a magnetar central engine. The rest of the bursts were consistent with having a black hole as the central engine. Sharma et al. (2021) analyzed the sample of GRBs detected by Fermi with measured redshift. They calculated the beaming corrected isotropic gamma-ray energies ( $E_{\text{beam,iso}}$ ) and compared them with the predicted maximum energy production of the magnetar and identified GRBs with black hole central engines. For GRB 190530A,  $E_{\text{beam,iso}} = (1 - \cos 3^\circ.81) \times 1.43 \times 10^{54} \text{ erg} = 3.16 \times 10^{51} \text{ erg}$ , and this value is approximately the same as the average energy of  $E_{\text{beam,iso}} = 1.9 \pm 4.2 \times 10^{51} \text{ erg}$  from Sharma et al. (2021). Furthermore, taking the “double-tracking” spectral evolution pattern both for  $E_p$  and  $\alpha$  into account, the black hole model is preferred as the engine of GRB 190530A.

### Acknowledgment

We acknowledge the support of the staff of the Xinglong 2.16 m telescope. We thank the anonymous referee for helpful recommendations to enhance this work. This work was partially supported by the Open Project Program of the Key Laboratory of Optical Astronomy, National Astronomical Observatories, Chinese Academy of Sciences. This work is supported by the National Key R&D Program of China (grant No. 2021YFA0718500), the National Natural Science Foundation of China (grant Nos. U1938201, 12103055, 11863007 and 11973055), the Guangxi Science Foundation (grant No. 2018GXNSFGA281007), the Innovation Project of Guangxi Graduate Education (grant No. YSCW2019050), and the Teaching reform project of Guangxi Higher Education (grant No. 2019JGZ102).

### ORCID iDs

Xiang-Gao Wang, <https://orcid.org/0000-0001-8411-8011>  
 Li-Ping Xin <https://orcid.org/0000-0002-9422-3437>  
 Bing Li <https://orcid.org/0000-0002-0238-834X>

Qi Luo <https://orcid.org/0000-0003-1853-7810>  
 Cheng-Kui Li <https://orcid.org/0000-0001-5798-4491>  
 Shao-Lin Xiong <https://orcid.org/0000-0002-4771-7653>  
 Ling-Jun Wang <https://orcid.org/0000-0002-8352-1359>  
 Li-Ming Song <https://orcid.org/0000-0003-0274-3396>  
 En-Wei Liang <https://orcid.org/0000-0002-7044-733X>  
 Shuang-Nan Zhang <https://orcid.org/0000-0001-5586-1017>

### References

- Amati, L. 2006, *MNRAS*, **372**, 233  
 Amati, L., Frontera, F., Tavani, M., et al. 2002, *A&A*, **390**, 81  
 Arnaud, K. A. 1996, in ASP Conf. Ser., 101, *Astronomical Data Analysis Software and Systems V*, ed. G. H. Jacoby & J. Barnes (San Francisco, CA: ASP), 17  
 Atwood, W. B., Abdo, A. A., Ackermann, M., et al. 2009, *ApJ*, **697**, 1071  
 Band, D., Matteson, J., Ford, L., et al. 1993, *ApJ*, **413**, 281  
 Band, D. L. 1997, *ApJ*, **486**, 928  
 Belkin, S. & IKI GRB FuN Collaboration 2019, GCN, 24712, 1  
 Belkin, S., Pozanenko, A., Inasaridze, R. Y., et al. 2019, GCN, 24698, 1  
 Biltzinger, R., Kunzweiler, F., Berlato, F., Burgess, J., & Greiner, J. 2019, GCN, 24677, 1  
 Bissaldi, E., & Meegan, C. 2019, GCN, 24692, 1  
 Burlon, D., Ghirlanda, G., Ghisellini, G., Greiner, J., & Celotti, A. 2009, *A&A*, **505**, 569  
 Burlon, D., Ghirlanda, G., Ghisellini, G., et al. 2008, *ApJL*, **685**, L19  
 Burrows, D. N., Hill, J. E., Nousek, J. A., et al. 2005, *SSRv*, **120**, 165  
 Cenko, S. B., Kasliwal, M., Harrison, F. A., et al. 2006, *ApJ*, **652**, 490  
 Cheng, L. X., Ma, Y. Q., Cheng, K. S., Lu, T., & Zhou, Y. Y. 1995, *A&A*, **300**, 746  
 Dai, Z. G., & Lu, T. 1998, *PhRvL*, **81**, 4301  
 Dai, Z. G., Wang, X. Y., Wu, X. F., & Zhang, B. 2006, *Sci*, **311**, 1127  
 Eichler, D., Livio, M., Piran, T., & Schramm, D. N. 1989, *Natur*, **340**, 126  
 Evans, P. A., Beardmore, A. P., Page, K. L., et al. 2009, *MNRAS*, **397**, 1177  
 Evans, P. A., Willingale, R., Osborne, J. P., et al. 2010, *A&A*, **519**, A102  
 Gehrels, N., Chincarini, G., Giommi, P., et al. 2004, *ApJ*, **611**, 1005  
 Götz, D., Covino, S., Hascoët, R., et al. 2011, *MNRAS*, **413**, 2173  
 Gupta, R., Gupta, S., Chattopadhyay, T., et al. 2022, *MNRAS*, **511**, 1694  
 Han, X., Xiao, Y., Zhang, P., et al. 2021, *PASP*, **133**, 065001  
 Huang, L. Y., Wang, X. G., Zheng, W., et al. 2018, *ApJ*, **859**, 163  
 Ito, H., Matsumoto, J., Nagataki, S., et al. 2019, *NatCo*, **10**, 1504  
 Kann, D. A. 2019, GCN, 24763, 1  
 Kann, D. A., Izzo, L., de Ugarte Postigo, A., et al. 2019a, GCN, 24684, 1  
 Kann, D. A., Izzo, L., de Ugarte Postigo, A., et al. 2019b, GCN, 24700, 1  
 King, A., O’Brien, P. T., Goad, M. R., et al. 2005, *ApJL*, **630**, L113  
 Koshut, T. M., Kouveliotou, C., Paciesas, W. S., et al. 1995, *ApJ*, **452**, 145  
 Kumar, B., & Pandey, S. B. 2019, GCN, 24729, 1  
 Kumar, P., & Zhang, B. 2015, *PhysRep*, **561**, 1  
 Lazzati, D. 2005, *MNRAS*, **357**, 722  
 Lei, W. H., Zhang, B., & Liang, E. W. 2013, *ApJ*, **765**, 125  
 Li, L., Geng, J. J., Meng, Y. Z., et al. 2019, *ApJ*, **884**, 109  
 Li, L., Wang, X. G., Zheng, W., et al. 2020, *ApJ*, **900**, 176  
 Li, L., Wu, X. F., Lei, W. H., et al. 2018, *ApJS*, **236**, 26  
 Liu, T., Gu, W. M., Xue, L., & Lu, J. F. 2007, *ApJ*, **661**, 1025  
 Liu, T., Song, C. Y., Zhang, B., Gu, W. M., & Heger, A. 2018, *ApJ*, **852**, 20  
 Longo, F., Racusin, J. L., Omodei, N., & Bissaldi, E. 2019, GCN, 24679, 1  
 Lü, H. J., & Zhang, B. 2014, *ApJ*, **785**, 74  
 Lu, R. J., Liang, Y. F., Lin, D. B., et al. 2018, *ApJ*, **865**, 153  
 Luo, Q., Liao, J. Y., Li, X. F., et al. 2020, *JHEAP*, **27**, 1  
 MacFadyen, A. I., & Woosley, S. E. 1999, *ApJ*, **524**, 262  
 Masada, Y., Kawanaka, N., Sano, T., & Shibata, K. 2007, *ApJ*, **663**, 437  
 Meegan, C., Lichti, G., Bhat, P. N., et al. 2009, *ApJ*, **702**, 791  
 Melandri, A., D’Avanzo, P., Tohuvavohu, A., et al. 2019, GCN, 24689, 1  
 Metzger, B. D., Piro, A. L., & Quataert, E. 2008, *MNRAS*, **390**, 781  
 Moskvitin, A. S., & Uklein, R. I. 2019, GCN, 24708, 1  
 Narayan, R., Paczynski, B., & Piran, T. 1992, *ApJL*, **395**, L83  
 Narayan, R., Piran, T., & Kumar, P. 2001, *ApJ*, **557**, 949

- Norris, J. P., Marani, G. F., & Bonnell, J. T. 2000, *ApJ*, 534, 248  
 Norris, J. P., Share, G. H., Messina, D. C., et al. 1986, *ApJ*, 301, 213  
 Paczynski, B. 1986, *ApJ*, 308, L43  
 Paczyński, B. 1998, *ApJL*, 494, L45  
 Paczynski, B., & Rhoads, J. E. 1993, *ApJL*, 418, L5  
 Popham, R., Woosley, S. E., & Fryer, C. 1999, *ApJ*, 518, 356  
 Rees, M. J., & Meszaros, P. 1994, *ApJL*, 430, L93  
 Romano, P., Campana, S., Chincarini, G., et al. 2006, *A&A*, 456, 917  
 Rowlinson, A., Gompertz, B. P., Dainotti, M., et al. 2014, *MNRAS*, 443, 1779  
 Rowlinson, A., O'Brien, P. T., Metzger, B. D., Tanvir, N. R., & Levan, A. J. 2013, *MNRAS*, 430, 1061  
 Schlafly, E. F., & Finkbeiner, D. P. 2011, *ApJ*, 737, 103  
 Sharma, V., Iyyani, S., & Bhattacharya, D. 2021, *ApJL*, 908, L2  
 Song, C. Y., Liu, T., Gu, W. M., & Tian, J. X. 2016, *MNRAS*, 458, 1921  
 Song, X. Y., Xiong, S. L., Zhang, S. N., et al. 2022, *ApJS*, 259, 46  
 Spruit, H. C., Daigne, F., & Drenkhahn, G. 2001, *A&A*, 369, 694  
 Stetson, P. B. 1987, *PASP*, 99, 191  
 Troja, E., Rosswog, S., & Gehrels, N. 2010, *ApJ*, 723, 1711  
 Turpin, D., Wu, C., Han, X. H., et al. 2020, *RAA*, 20, 013  
 Uhm, Z. L., & Zhang, B. 2016, *ApJ*, 825, 97  
 Uhm, Z. L., Zhang, B., & Racusin, J. 2018, *ApJ*, 869, 100  
 Ukwatta, T. N., Dhuga, K. S., Stamatikos, M., et al. 2012, *MNRAS*, 419, 614  
 Usov, V. V. 1992, *Natur*, 357, 472  
 Virgili, F. J., Qin, Y., Zhang, B., & Liang, E. 2012, *MNRAS*, 424, 2821  
 Wang, X. G., Zhang, B., Liang, E. W., et al. 2018, *ApJ*, 859, 160  
 Wang, X. Y., & Mészáros, P. 2007, *ApJ*, 670, 1247  
 Wei, J., Cordier, B., Antier, S., et al. 2016, arXiv:1610.06892  
 Willingale, R., Starling, R. L. C., Beardmore, A. P., Tanvir, N. R., & O'Brien, P. T. 2013, *MNRAS*, 431, 394  
 Woosley, S. E. 1993, *ApJ*, 405, 273  
 Xin, L. P., Li, G. W., Zhang, R. S., et al. 2019a, GCN, 24688, 1  
 Xin, L. P., Zhang, J. B., Li, G. W., et al. 2019b, GCN, 24697, 1  
 Yi, Q. B., Xiao, S., Luo, Q., et al. 2019, GCN, 24714, 1  
 Yonetoku, D., Murakami, T., Nakamura, T., et al. 2004, *ApJ*, 609, 935  
 Yonetoku, D., Murakami, T., Tsutsui, R., et al. 2010, *PASJ*, 62, 1495  
 Zhang, B., & Mészáros, P. 2002, *ApJ*, 581, 1236  
 Zheng, T. C., Li, L., Zou, L., & Wang, X. G. 2021, *RAA*, 21, 300